Selective nonreciprocal localization of flat magnonic modes induced by a periodic Dzyaloshinskii-Moriya interaction

J. Flores-Farías, D. Cortés-Ortuño, F. Brevis, P. Landeros, and R. A. Gallardo*
Departamento de Física, Universidad Técnica Federico Santa María, Avenida España 1680, Valparaíso, Chile

(Received 14 September 2023; revised 19 December 2023; accepted 22 January 2024; published 21 February 2024)

Spin waves excited in periodically modulated magnetic nanomaterials, known as magnonic crystals, exhibit characteristic band structures. These bands can be tuned by material engineering and have been attractive for potential spin-based applications. When periodic nanomaterials with handedness are introduced, spin waves inherit the chiral feature in their behavior and manifest an exciting range of novel physics, including asymmetric and unidirectional propagation, low-frequency magnonic flat bands, and indirect band gaps. This study investigates the properties of these chiral magnonic excitations. The analysis is performed in ferromagnetic films patterned with nanowires of two different materials that produce periodically modulated perpendicular magnetic anisotropy and interfacial antisymmetric exchange (Dzyaloshinskii-Moriya interaction). The low-frequency flat modes are studied using a magnonic localization diagram that distinguishes the spatial confinement degree in zones with and without antisymmetric exchange. An analytical expression is derived for the transition region in the localization diagram that outlines the zones where magnonic confinement occurs. The findings reveal the presence of flat modes with nonreciprocal magnetization oscillation amplitudes between waves with opposite propagation directions when the spin-wave localization occurs in regions with Dzyaloshinskii-Moriya interaction. Conversely, reciprocal oscillation amplitudes are observed when modes localize in the nanowires with perpendicular anisotropy. Micromagnetic simulations demonstrate the amplitude asymmetry of the flat modes, yielding perfect agreement with the theoretical predictions. This paper provides a deeper understanding of the behavior of spin-wave modes in chiral magnonic crystals and establishes a method to control their associated magnonic bands for designing spin-wave-based nanodevices.

DOI: 10.1103/PhysRevB.109.054423

I. INTRODUCTION

Spin waves (SWs) are elementary excitations of magnetically ordered materials, which emerge from the collective motion of localized magnetic moments [1–3]. The research on the magnetization dynamics in nanomaterials has unveiled a range of linear and nonlinear phenomena, such as ferromagnetic resonance [4,5], parametric spin pumping [6], and three and four-magnon scattering [7], for instance. At the same time, solitons and breathers have been observed as localized, stable wave packets that propagate without changing their shape [8,9]. It has been shown that SWs have numerous advantages over conventional electric transport, including reduced energy consumption, rapid information processing, nonvolatility, and scalability down to the nanoscale [10,11]. As a result, it has been possible to confine and manipulate SWs for the design of compact, high-performance, and densely integrated magnon-based devices and circuits [12–15], that have the potential to revolutionize how information is processed and stored [16].

Recently, experimental evidence has attracted attention to a specific kind of nanomagnets with broken inversion symmetry, which can occur at the interface between a heavy-metal layer and a ferromagnetic film [17–20], or at the crystal structure, as in the case of noncentrosymmetric magnets [21,22]. The lack of inversion symmetry induces an antisymmetric exchange interaction between neighboring spins, known as the Dzyaloshinskii-Moriya interaction (DMI) [23,24]. A crucial characteristic of SWs propagating in a material with DMI is their nonreciprocal behavior under a wave-vector inversion [25–27]. Specifically, two counterpropagating waves at the same frequency exhibit different wavelengths [28,29]. The effect of SW nonreciprocity is not exclusive to materials with DMI. Nonlocal dipolar interactions can also induce a DM-like coupling in a Damon-Eshbach configuration when the spatial symmetry is broken across the film thickness, as happens in oppositely magnetized bilayers [30–36]. A similar effect is observed in curved magnetic structures [37–41]. The asymmetry in the SW dispersion has been relevant for envisioning various technological applications, including magnonic diodes, magnonic circulators, isolators, phase shifters, and logic devices [42–44]. Indeed, under certain conditions, the SW dispersion can exhibit unidirectionality in specific frequency ranges, allowing waves to propagate unaffected by reflections from defects or imperfections [41,45–48].

A practical method to manipulate SW bands in a magnetic system is by introducing an artificial periodicity, for instance, by patterning regions with alternating ferromagnetic materials. Then, the magnonic band structure exhibits characteristic forbidden-and-allowed frequency bands [49–51]. These engineered periodic architectures, commonly called magnonic crystals (MCs), allow the tailored control

*rodolfo.gallardo@usm.cl

and manipulation of SWs. Hence, they have a strong potential in spin-based nanotechnologies [52–54]. For example, band gaps could be used to design magnonic filters and isolators, which can selectively transmit or suppress waves within specific frequencies [55–57]. Possible designs of MCs include geometric modulation [58–62], bicomponents [63–66], and periodic coupling of different magnetic materials [32,67,68].

Under periodic exchange or dipolar interactions, the spin excitations exhibit a symmetric frequency dispersion in ultrathin ferromagnetic films, with magnonic band gaps opening at the boundaries of the Brillouin zone. This symmetry is broken when a chiral interaction is introduced [69]. For instance, patterning heavy-metal (HM) stripes in contact with a continuous film produces periodic regions with interfacial DMI owing to the large spin-orbit coupling. Such a system exhibits low-frequency flat bands represented by localized magnetic excitations beneath the HM stripes. Such phenomenon was predicted theoretically [70,71] and has recently been confirmed experimentally [72]. Additionally, indirect band gaps can be observed for the high-frequency modes, with the gaps shifted from the edges of the Brillouin zone [70,73]. Flat bands originate from the reduction of the internal field in the regions with DMI (the ones in contact with the HM stripes), leading to the robust localization of SW modes in those areas, where standing waves emerge with almost zero group velocity. According to this, flat bands can also be induced by a periodic perpendicular surface anisotropy because it decreases the internal field in an in-plane magnetized film. In contrast to the localization of flat SW modes caused by anisotropy, in materials with DMI these dispersionless modes have chiral attributes, which imply that the magnetization oscillation amplitude should be wave-vector dependent. Phenomena resulting from the chirality and localization of SW modes in an MC have yet to be fully understood. The analysis of these physical processes is relevant to deepen the knowledge of the physics of confined SWs in chiral periodic nanomaterials and, hence, to extend the possibilities of tuning their band structure.

This study focuses on a chiral one-dimensional magnonic crystal based on an ultrathin film coupled with an array of HM nanostripes, which generate a periodic interfacial DMI. These HM nanostripes alternate with a second array of stripes of a lighter metal, such as Ru [72]. The lighter metal regions (without interfacial DMI) generate a significant perpendicular surface anisotropy that is also periodic. This system exhibits flat bands, and the behavior of the lowest-frequency band is analyzed as a function of both anisotropy and DMI strength. A localization diagram is calculated to analyze the SW profiles of such a lowest-frequency flat band. Analytical expressions that shed light on the transition between magnetization excitations localized inside and outside the DMI regions are derived. Nonreciprocal SW amplitudes for the flat modes are predicted when the Dzyaloshinskii-Moriya interaction dominates, owing to its chiral nature. Conversely, the low-frequency flat bands exhibit reciprocal magnetization amplitudes when the anisotropy increases and the SWs localize beneath the lighter metals. Micromagnetic simulations are performed to substantiate the validity of the proposed model.

II. THEORY

The investigated system comprises a ferromagnetic ultrathin film coupled with an alternating array of heavy-metal nanostripes and a second group of nanostripes made of a lighter metal. At the interface between the magnetic film and these two types of materials, either a perpendicular anisotropy or an interfacial Dzyaloshinskii-Moriya interaction arises. The ferromagnetic material chosen is CoFeB, while Pt is selected as the reference HM due to its high spin-orbit coupling [74–76], which induces a substantial interfacial DMI strength D in ultrathin magnetic films [28,29]. In regions without HMs, the ferromagnet is coupled with a lighter material that induces perpendicular magnetic anisotropy. According to experimental observations, a prominent perpendicular anisotropy has been observed in multilayer systems, such as CoFeB/Ta [77], CoFeB/Pt [78], and CoFeB/Ru [72,79–82]. Thus, in areas without HMs, the metal Ru is used as a reference to obtain a significant perpendicular surface anisotropy. Note that a finite perpendicular anisotropy in the CoFeB/Pt interface is also expected [78]. Nevertheless, for the sake of simplicity, such an anisotropy will be assumed null in this paper. In the case of considering an anisotropy in the Pt zone, the results remain unaffected by a rescaling of the anisotropy value in ruthenium, namely $H_s^{\mathrm{Ru}} \to H_s^{\mathrm{Ru}} - H_s^{\mathrm{Pt}}$, provided the perpendicular anisotropy in Ru surpasses that in Pt. Figure 1(a) shows an overview of the one-dimensional chiral MC defined for the study.

The calculations assume that the equilibrium magnetization $\mathbf{M}_0$ lies in the film plane, along the x axis and parallel to the external field $\mathbf{H}_0$. The SW propagation occurs along the z axis, corresponding to Damon-Eshbach modes with a wave vector $\mathbf{k} = k\hat{z}$. The period of the MC is denoted by a, and the width of the Pt nanostripes is represented by w [see Fig. 1(a)]. A theory based on the plane-wave method (PWM) is employed to calculate the magnonic band structure [70–72], which considers Zeeman, exchange, dipolar, perpendicular anisotropy, and interfacial DM interactions. In the theoretical description, zero damping is assumed because, in the linear regime, damping does not exert a significant influence on the band structure. However, it is important to note that this damping will impact the attenuation length of the waves. For Pt/CoFeB the damping increment is well-known [83,84], resulting in distinct lifetimes for modes propagating in the Pt or Ru zones. To investigate the nature of the magnonic flat modes, the function

$$\Gamma_{\eta}^{(\nu)} = \frac{1}{w_{\eta}} \int_{0}^{w_{\eta}} |\mathbf{m}| dz, \tag{1}$$

is defined to quantify the degree of localization of the SWs in the regions in contact with Ru ($\eta = \mathrm{Ru}$) and Pt ($\eta = \mathrm{Pt}$). Parameter ν represents the band number, being $\nu = 0$ the lowest-frequency mode, and $\nu > 0$ the higher-order modes. The function $\Gamma_{\eta}^{(\nu)}$ represents the spatially averaged amplitude of the normalized dynamic magnetization $\mathbf{m}$. These averages are computed within the CoFeB zones in contact with the Ru and Pt nanostripes. Such zones are defined by the widths $w_{\mathrm{Ru}} = a - w$ and $w_{\mathrm{Pt}} = w$, respectively, as illustrated in Fig. 1(a). In Eq. (1), $|\mathbf{m}| = \sqrt{m_z^2(\mathbf{r}, t) + m_y^2(\mathbf{r}, t)}$, where

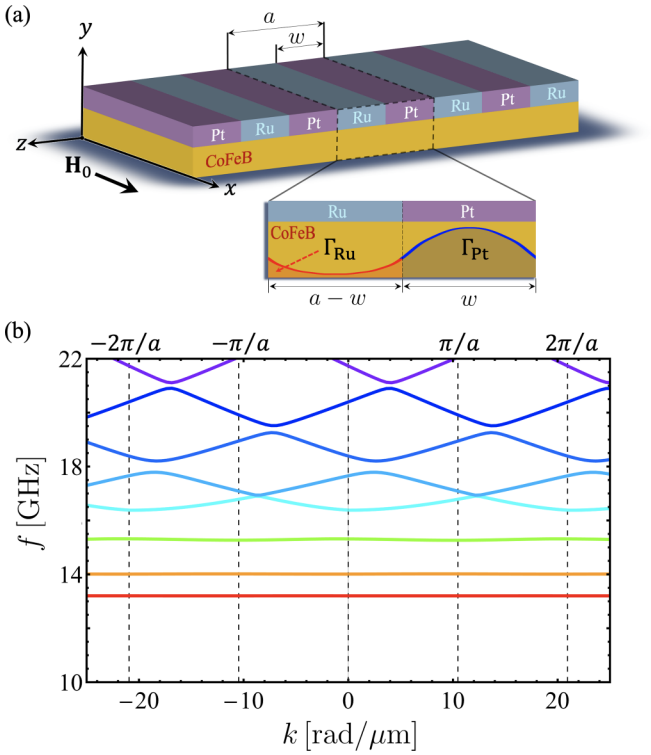

FIG. 1. (a) Illustration of a one-dimensional chiral magnonic crystal (MC) consisting of alternating ruthenium (Ru) and platinum (Pt) nanowires of width w, coupled with a continuous layer of CoFeB and thickness $d = 1$ nm. The unit cell of size $a = 2w$ and the Γ_η function, related to the spatially averaged amplitude of the dynamic magnetization, are illustrated. The magnetization of the MC is saturated with an external magnetic field $\mathbf{H}_0 = H_0\hat{x}$ such that spin waves are excited in the Damon-Eshbach configuration $\mathbf{k} = k\hat{z}$. (b) The calculated SW band structure, obtained with $\mu_0 H_s = 200$ mT, $M_s = 900$ kA/m, $D = 2.5$ mJ/m^2, $w = 150$ nm, and $a = 300$ nm, reveals the formation of flat magnonic bands.

$m_z(\mathbf{r}, t)$ and $m_y(\mathbf{r}, t)$ represent the in-plane and out-of-plane normalized dynamic magnetization components, respectively. As $\Gamma_\eta^{(\nu)}$ is directly proportional to the area under the curve describing $|\mathbf{m}|$ [see Fig. 1(a)], a value of $\Gamma_{\text{Ru}}^{(\nu)} = 1$ ($\Gamma_{\text{Pt}}^{(\nu)} = 1$) indicates a complete localization of the SW modes under the Ru (Pt) zone. A measure of the magnon localization can be done using the following function:

$$\Delta\Gamma^{(\nu)} = \Gamma_{\text{Pt}}^{(\nu)} - \Gamma_{\text{Ru}}^{(\nu)}. \tag{2}$$

In the case of $\Delta\Gamma^{(\nu)} = \pm 1$, the modes exhibit a strong localization in the Pt ($\Delta\Gamma^{(\nu)} = +1$) or Ru ($\Delta\Gamma^{(\nu)} = -1$) region. The primary characteristic of the dynamics of the chiral MC depicted in Fig. 1(a) is the formation of flat magnonic bands [70–72]. It can be seen from Fig. 1(b) that the low-frequency modes exhibit flat bands. The analysis focuses on the lowest-frequency mode ($\nu = 0$) because it is more likely to show a nondispersive character [70]. In the case of high-frequency modes, the exchange interaction starts to dominate, leading to dispersive SW bands. This is shown in Fig. 1(b), where in this example the dispersive modes start from the fourth lowest frequency band. In what follows, it will be denoted that $\Gamma^{(0)} = \Gamma$, and $\Delta\Gamma^{(0)} = \Delta\Gamma$ for simplicity.

III. RESULTS

For the calculations, the exemplary ferromagnetic material under investigation, CoFeB, is characterized by $A_{\text{ex}} = 15$ pJ/m and a gyromagnetic ratio of $\gamma = 186.6$ GHz/T. The saturation magnetization is varied between 900 and 1500 kA/m, while the remaining parameters associated with CoFeB are held constant. The calculations are performed using an external field in the range $\mu_0 H_0 = 50$ to 250 mT and a film thickness of $d = 1$ nm. The band structure in the Damon-Eshbach configuration is presented in Fig. 1(b). The parameters used are $a = 300$ nm, $w = 150$ nm, $\mu_0 H_0 = 250$ mT, a perpendicular anisotropy field $\mu_0 H_s = 200$ mT, $M_s = 900$ kA/m, and a DMI strength $D = 2.5$ mJ/m^2. Three nondispersive low-frequency modes (flat bands) are obtained in this case. These flat branches exhibit strong localization within specific regions of the magnetic material, which depends on the interplay between anisotropy, saturation magnetization, and DMI strengths.

To study the localization of the flat modes, the parameter $\Delta\Gamma$ obtained from the PWM calculations is analyzed as a function of $\mu_0 H_s$ and D. The results are illustrated in Fig. 2, where three different saturation magnetization values and two periods have been considered. The top row corresponds to the magnonic crystals with period $a = 300$ nm, while the bottom row represents $a = 100$ nm. All calculations consider the case where the Ru and Pt have the same widths, $w_{\text{Ru}} = w_{\text{DM}} = a/2$. For positive values of $\Delta\Gamma$ (shown in purple), the flat SW modes tend to localize in the regions underneath Pt. In contrast, surface anisotropy dominates for negative values of $\Delta\Gamma$ (shown in slate blue), leading to the localization of spin excitations beneath the Ru nanowires. From the diagrams presented in Fig. 2, it can be observed that both anisotropy and interfacial DMI can induce highly localized states with $\Delta\Gamma = \pm 1$. This localization is closely connected to the formation of flat bands because wave propagation is restricted.

The transition from $\Delta\Gamma = 1$ to $\Delta\Gamma = -1$ (or vice versa) depends on the magnitudes of D and $\mu_0 H_s$. At large values of these magnetic parameters, the transition is abrupt, while at small values, the transition becomes smooth (white zones). These white zones broaden with M_s, evidenced by the contour lines evaluated at $\Delta\Gamma = \pm 0.5$, ± 0.6, and 0. This behavior is attributed, firstly, to the fact that the DMI strength follows a D/M_s trend in the SW dispersion [27,70]. As a result, when M_s increases, the influence of the DMI diminishes. Secondly, the white zone is a region where neither DMI nor anisotropy dominates. In this scenario, the magnetic excitations are distributed throughout the unit cell, preventing them from being confined to specific zones of the magnetic layer. The two combined effects produce a gradual SW-localization transition shown by a white region in Fig. 2, where $\Delta\Gamma \approx 0$. Note that the white zone widens as the period is reduced, as can be seen comparing the cases $a = 300$ nm and $a = 100$ nm. This behavior is explained by the fact that as the period decreases, the modes are forced to oscillate in smaller regions, thus enhancing the exchange interaction that promotes a dispersive character of the SWs. In other words, the low-frequency mode transforms from flat to dispersive as the period decreases.

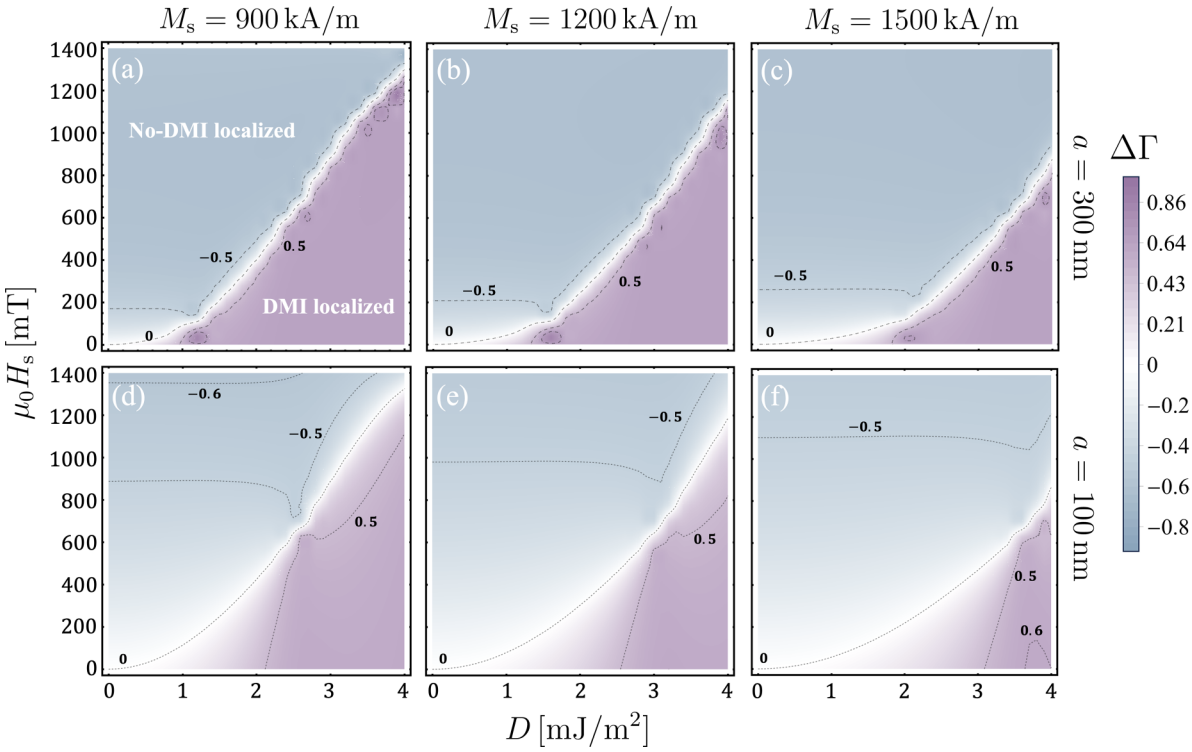

FIG. 2. Magnonic localization diagrams for the lowest-frequency mode. The color code represents $\Delta\Gamma$, the difference in the spatially averaged amplitudes of the normalized dynamic magnetization beneath Pt and Ru, as a function of the anisotropy field and DMI strength. For $\Delta\Gamma > 0$ ($\Delta\Gamma < 0$), the spin waves are localized in the Pt (Ru) regions, while for $\Delta\Gamma \approx 0$, the magnetic excitations are localized in both zones. Contour lines for values $\Delta\Gamma = \pm 0.5, \pm 0.6$, and 0, are depicted as references. Diagrams in (a)–(c) are calculated for a period $a = 300\,\mathrm{nm}$, while in (d)–(f) $a = 100\,\mathrm{nm}$. For the columns, the saturation magnetization is 900, 1200, and 1500 kA/m. In all cases, $\mu_0 H_0 = 250$ mT and $w = a/2$ (filling fraction 0.5).

Spin-wave profiles have been computed for specific values of D and $\mu_0 H_s$. Figure 3(a) illustrates the localization diagram for $M_s = 900$ kA/m and $a = 300\,\mathrm{nm}$. At point P_1, a significant localization of the SWs in the regions adjacent to Ru is obtained, while at points P_2 and P_4, the modes are mostly active underneath Pt, where DMI dominates. Notice that the temporal evolution of standing waves in the zones with DMI is unusual, where the nodes move as time passes [70,85]. One distinctive point in the diagram is point P_3, where neither anisotropy nor DMI dominates. As a result, magnetization oscillations are present throughout the entire unit cell but with an anomalous spatio-temporal profile, as depicted in the subplot of point P_3 of Fig. 3(b).

The dispersion relation of a continuous ferromagnetic film (nonperiodic) is studied to comprehend the transition between the two types of localizations (represented by the slate blue to purple colors). When considering solely the effects of anisotropy, the frequency of the SW dispersion of an extended film exhibits a minimum at $k = 0$ ($f = f_0^{H_s}$), as illustrated in Fig. 3(c). The occurrence of this minimum at $k = 0$ stems from considering the scenario where $\mu_0 M_s > \mu_0 H_s$ in the calculations. When $\mu_0 H_s$ overcomes $\mu_0 M_s$, the minima of the spin-wave dispersion are given at finite wave vectors [86]. Nevertheless, if $\mu_0 H_s$ is only slightly larger than $\mu_0 M_s$, the frequency difference between the true minima and $f(k = 0)$ is negligibly small. In Fig. 3(c), the dashed, dot-dashed, and dotted lines represent the cases evaluated at $D = 0$, corresponding to the anisotropies of points P_1 ($\mu_0 H_s = 1200$ mT), P_3 ($\mu_0 H_s = 613$ mT), and P_4 ($\mu_0 H_s = 200$ mT), respectively. However, in the presence of DMI only, with zero anisotropy, the frequency of the waves has a minimum at a finite wave vector k_c, but only for a specific wave vector direction. This behavior is illustrated in Fig. 3(c), where the solid curve represents the case of a continuous film with $D = 2.5\,\mathrm{mJ/m^2}$ and $\mu_0 H_s = 0$. By comparing the minima of the dispersion relations shown in Fig. 3(c) (f_0^{DM} and $f_0^{H_s}$), one can anticipate the nature of the SW localization of the flat bands in a magnonic crystal. For instance, analyzing the minimum of the dispersion only with DMI (solid line) f_0^{DM}, and the minimum of the dispersion only with surface anisotropy $f_0^{H_s}$, evaluated at $\mu_0 H_s = 200$ mT (dotted curve), one can observe that the film with DMI exhibits a lower frequency minimum. Therefore, in a nanoscale magnetic film composed of periodic zones with coexisting anisotropy (with $\mu_0 H_s = 200$ mT) and DMI (with $D = 2.5\,\mathrm{mJ/m^2}$) regions, it is expected that the lowest-frequency flat mode is primarily localized in the regions underneath the HM nanostripes since such an environment is compatible with the low-frequency spin excitations. As the anisotropy increases, the frequency minimum $f_0^{H_s}$ decreases, resulting in $f_0^{H_s} < f_0^{\mathrm{DM}}$, as shown by the solid and dashed lines in Fig. 3(c). Consequently, the low-frequency modes are more likely to localize beneath the Ru zones, where the anisotropy dominates. The analysis indicates that at the critical state $f_0^{H_s} = f_0^{\mathrm{DM}}$, the anisotropy and interfacial DM

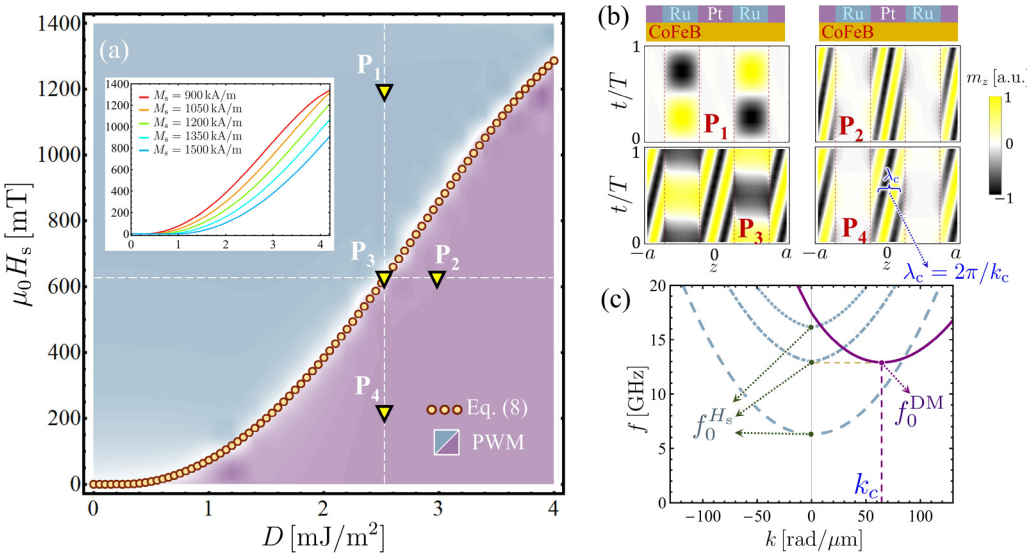

FIG. 3. (a) Magnon localization diagram for the lowest-frequency mode evaluated for $M_s = 900$ kA/m, $\mu_0 H_0 = 250$ mT and period $a = 300$ nm, so the filling fraction is 0.5. Color code (see Fig. 2) results are obtained from the PWM calculations, while the circle dots correspond to the analytical formula given by Eq. (8). The triangles, defined as (D [mJ/m^2], $\mu_0 H_s$ [mT]), correspond to the points $P_1 = (2.5, 1200)$, $P_2 = (3, 613)$, $P_3 = (2.5, 613)$, and $P_4 = (2.5, 200)$. (b) Spatiotemporal profiles of the spin-wave modes evaluated at the points P_1–P_2, where T is the temporal period of the magnetization oscillations. In P_1, the modes are localized at the Ru zones, while in points P_2 and P_4, the magnetic excitations live at the Pt areas. Point P_3 describes cases where the excitations are simultaneously beneath the Pt and Ru nanostripes. (c) Spin-wave dispersions of an effective continuous film without interfacial DMI ($D = 0$) and evaluated at $\mu_0 H_s = 1200$ mT (dashed line), $\mu_0 H_s = 613$ mT (dot-dashed line), and $\mu_0 H_s = 200$ mT (dotted line). The solid line considers the case of an extended film with $D = 2.5$ mJ/m^2 and $\mu_0 H_s = 0$, where k_c is the critical wave vector at which the frequency is minimum.

interactions are equally important. This critical state should be consistent with point P_3 shown in Fig. 3(b), where $\Delta\Gamma$ approaches zero. To obtain an analytical expression for $f_0^{H_s}$ and f_0^{DM}, the spin-wave dispersion of the continuous film must be analyzed. In the case of a continuous film with perpendicular anisotropy and DMI, the SW dispersion is given by [27,70]

$$f = \frac{\gamma}{2\pi}\left[-\frac{2D}{M_s}k + \sqrt{\left(\mu_0 H_0 - \mu_0 H_s + D_{ex}k^2 + \mu_0 M_s e^{-\frac{d|k|}{2}}\right)\left(\mu_0 H_0 + D_{ex}k^2 + \mu_0 M_s\left(1 - e^{-\frac{d|k|}{2}}\right)\right)}\right], \tag{3}$$

where $D_{ex} = 2A_{ex}/M_s$, being A_{ex} the exchange constant. From Eq. (3), the frequency $f_0^{H_s}$, with $D = 0$ and $k = 0$, is readily determined, namely

$$f_0^{H_s} = (\mu_0\gamma/2\pi)\sqrt{H_0(H_0 + M_s - H_s)}. \tag{4}$$

On the other hand, it is necessary to realize some approximations to obtain an analytical expression for the dynamic state f_0^{DM} shown in Fig. 3(c). First, the limit $kd \ll 1$ is considered, so that the SW dispersion evaluated to $H_s = 0$ is

$$f^{DM} = \frac{\gamma}{2\pi}\left[\frac{(\mu_0 M_s)^2|k|d}{4\xi(k)} - \frac{2D}{M_s}k + \xi(k)\right], \tag{5}$$

where

$$\xi(k) = \sqrt{(\mu_0 H_0 + D_{ex}k^2)(\mu_0 H_0 + \mu_0 M_s + D_{ex}k^2)}. \tag{6}$$

Second, from the condition $df^{DM}/dk = 0$, an expression for the term k_c can be obtained. In order to obtain an analytical form for k_c, a parabolic behavior of the dispersion will be assumed so that Eq. (5) is expanded up to second order in the wave vector k. Thus, the critical wave vector obtained is

$$k_c = \frac{8D\sqrt{H_0(H_0 + M_s)} - d\mu_0 M_s^3}{4D_{ex}M_s(2H_0 + M_s)}. \tag{7}$$

Finally, replacing Eq. (7) into Eq. (5), the minimum of the dispersion, f_0^{DM} is obtained. As mentioned above, the condition $f_0^{H_s} = f_0^{DM}$ allows to obtain an expression for the dynamic state $\Delta\Gamma = 0$. Thus, by equating the frequency minima, and after some algebraic manipulations, a relationship between D and $\mu_0 H_s$ can be established at the transition point, resulting in

$$\mu_0 H_s(D) = \mu_0 M_s + \mu_0 H_0 - \mathcal{F}(D), \tag{8}$$

where

$$\mathcal{F}(D) = \frac{1}{\mu_0 H_0}\left[\frac{(\mu_0 M_s)^2|k_c|d}{4\xi(k_c)} - \frac{2D}{M_s}k_c + \xi(k_c)\right]^2. \tag{9}$$

The circles depicted in Fig. 3(a) correspond to the analytical formula given in Eq. (8), while the inset shows the evolution of $\mu_0 H_s(D)$ for different values of the saturation magnetization, reproducing the cases illustrated in Fig. 2. Therefore,

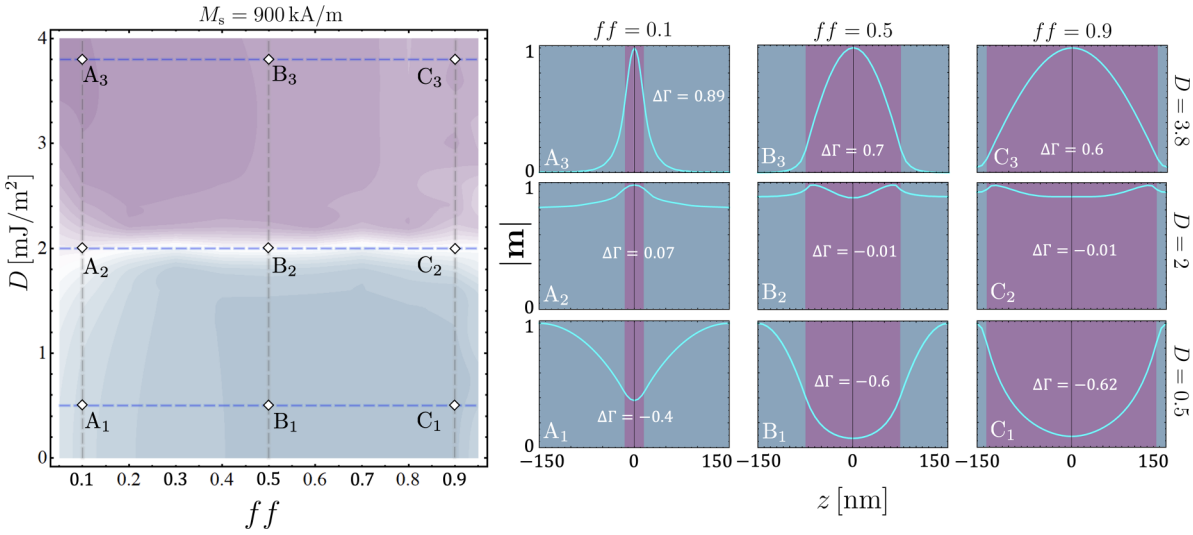

FIG. 4. The plot on the left shows a localization diagram (evaluated for the lowest-frequency band), illustrating the evolution of $\Delta\Gamma$ as a function of D and ff. A constant anisotropy field of $\mu_0 H_s = 400$ mT is used in the calculations. Similar to previous figures, the color map distinguishes whether the mode is localized in Pt or Ru (refer to Fig. 2). Spin-wave profiles, depicted by the absolute value of the dynamic magnetization $|\mathbf{m}|$, are computed for various points on the diagram, as illustrated in the right panels. Notably, at points A_2, B_2, and C_2, it is observed that the function $\Delta\Gamma \approx 0$, indicating that the mode is distributed almost equally between the Ru and Pt zones. In other cases, a notable localization in Ru (points A_1, B_1, and C_1) and Pt (points A_3, B_3, and C_3) is given.

an excellent agreement between the analytical formalism and the transition region computed via the PWM is found, which validates the expression obtained in Eq. (8). Furthermore, from the analysis of Fig. 3(c), one notices that the wavelengths λ_c of the modes excited underneath Pt [see point P_4 in Fig. 3(b)] are directly related to the critical wave vector k_c [see Eq. (7)] derived for the continuous film. Specifically, these wavelengths can be determined by $\lambda_c = 2\pi/k_c$. The match between the wavelengths evaluated at $k = k_c$ and one of the lowest-frequency modes in the chiral MC substantiates the derivation of Eq. (8). Furthermore, in Fig. 3(b), it is observed that the modes localized in the Ru zone (point P_1) have an infinite wavelength. This observation aligns with the concept presented in Fig. 3(c), where the lowest-frequency modes localized in Ru are linked to states with $k = 0$, resulting in $\lambda \to \infty$. Hence, concerning the nature of the flat modes, there is a direct relation between a continuous film and a chiral magnonic crystal.

One can observe that Eq. (8) is independent of the filling fraction $ff = w/a$, so if the width w is modified, the transition line should be similar to the one shown in Fig. 3 for $ff = 0.5$. To validate this hypothesis, the localization degree, denoted by $\Delta\Gamma$, is examined as a function of ff and D. This result is illustrated in Fig. 4, wherein the case with $\mu_0 H_s = 400$ mT is chosen as a reference. This analysis demonstrates that the expression $\mu_0 H_s(D)$ remains applicable even as the filling fraction changes. Here, the transition from positive to negative (or vice versa) values of $\Delta\Gamma$ is characterized by the zone with $\Delta\Gamma = 0$ (indicated by the white color), which remains independent of ff. The purple and slate blue colors exhibit a slight dependence on the filling fraction, as evident from the modulations of the white color in Fig. 4. Spin-wave profiles are also presented in Fig. 4 (see states A_1–A_3, B_1–B_3, and C_1–C_3), where the absolute value of the dynamic magnetization is plotted as a function of z. Notably, points A_2, B_2, and C_2 are consistent with Eq. (8) and represent the dispersive modes with similar localization in both Pt and Ru regions. Nonetheless, the filling fraction does influence the localization of the spin waves. For example, for low filling fractions, mode A_2 is localized both at Ru and at the center of the Pt nanowires (see Fig. 4), while for large filling fractions (modes B_2 and C_2), the modes localize in both regions but towards the edges of the Pt wires. The behavior shown in Fig. 4 does not change qualitatively as the anisotropy changes (not shown).

Another property of a chiral MC refers to the nonreciprocal properties of the magnetization oscillation amplitude for low-frequency flat modes. Owing to the chiral nature of the DMI coupling, it is inferred that the flat bands of modes localized underneath the HM nanostripes exhibit nonreciprocal amplitudes. Namely, by considering the SW dispersion with DMI of the continuous film shown in Fig. 3(c), it is expected that flat modes localized beneath Pt have a robust localization at positive wave vectors. On the other hand, at negative wave vectors, the magnetization oscillation amplitudes are smaller. This behavior implies that the system exhibits a more prominent occupation of these modes at positive k. In contrast, when anisotropy dominates over DMI, the flat modes are localized in the Ru zones, where the system is achiral, and, hence, the flat bands have similar intensities at negative and positive wave vectors since the SW dispersion for $D = 0$ is reciprocal.

Micromagnetic simulations using the MuMax3 code [71,72] have been performed to corroborate the predictions about the intensity of the SW modes. The simulations compute the Fourier amplitude of SW modes excited with a small alternating external field in wave vector and frequency space. Results of simulations are shown in Fig. 5. Here, the minima in spin-wave intensity at specific k values arise from numerical artifacts in the simulations, which are caused by

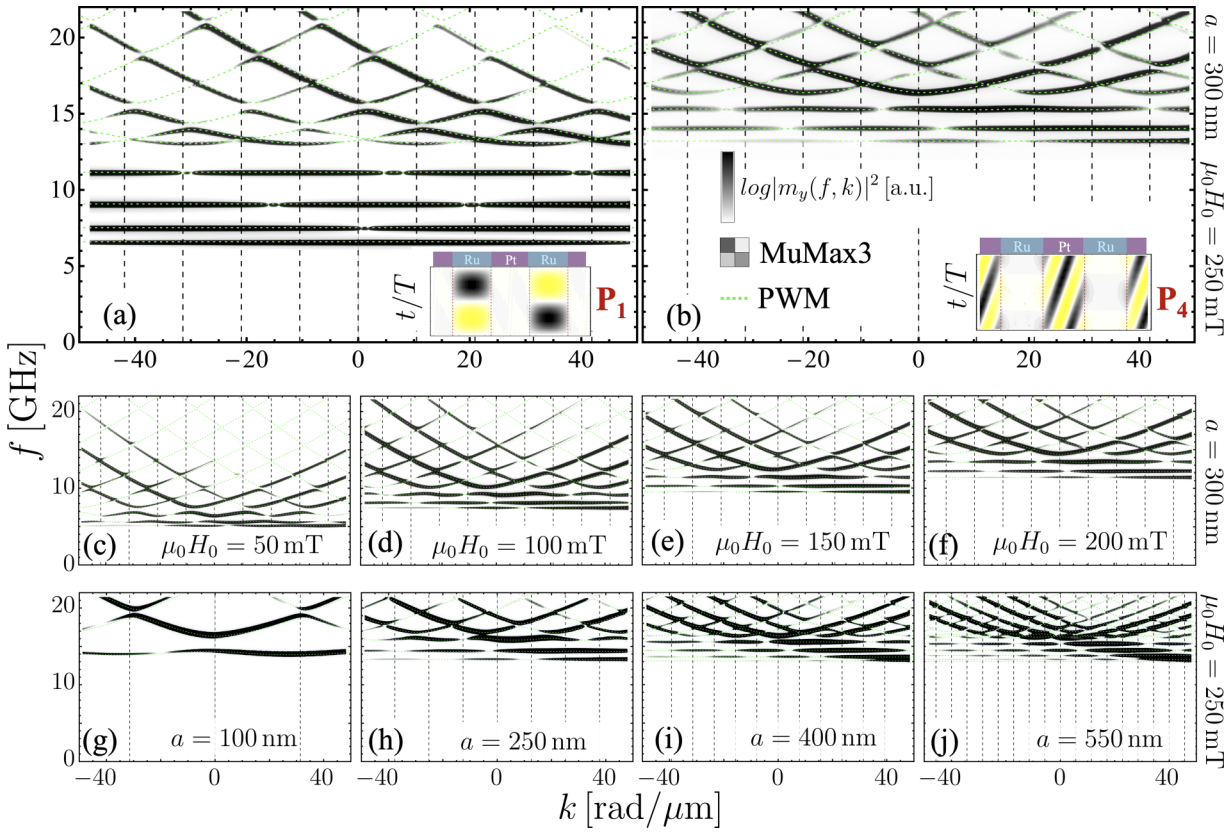

FIG. 5. Panels (a) and (b) illustrate the magnonic band structure associated with points P_1 and P_4 of Fig. 3(a). The dotted green lines represent the calculated dispersion, while the power spectrum of the MuMax3 simulations is depicted using gray scale. The insets display the spin-wave profiles for the lowest-frequency band evaluated at $k = 0$. In panel (a), a symmetric intensity of the simulated power spectrum is obtained under the inversion of the wave vector. At point P_4, panel (b), the low-frequency flat modes exhibit an amplitude asymmetry due to the influence of the interfacial Dzyaloshinskii-Moriya interaction. Panels (c)–(f) illustrate the variation of band structure as a function of external fields with a selected unit cell, whereas (g)–(j) exhibit band structures for different unit cells with a fixed external field. Vertical dotted lines illustrate the Brillouin zone edges. In all cases, $w = a/2$.

multiple factors such as the boundary conditions at the material interfaces (regions with and without DMI), the numerical discretization, and the definition of the excitation pulse. This effect has been reported in other studies such as Ref. [87], and might be avoided using an alternative frequency-space numerical method. The simulations are realized for the cases P_1 and P_4 (see Fig. 3). Figure 5(a) illustrates the simulated (and calculated) SW dispersion for point P_1, with the lowest-frequency flat mode localized beneath Ru. In this scenario, the simulations display a flat band with a reciprocal SW power-spectrum amplitude, in agreement with the theoretical picture. Conversely, at point P_4, where the DMI dominates, the flat band exhibits a nonreciprocal amplitude, as depicted in Fig. 5(b). Here, it is noted that the simulated flat modes have a stronger power-spectrum amplitude at positive wave vectors, which is consistent with the idea presented in Fig. 3(c) (see solid lines), where the minimum of the SW dispersion evaluated at a finite DMI strength happens at a positive k_c.

To complement the analysis of the amplitude asymmetry observed in the micromagnetic simulations, the period a and the external field are varied for the chiral flat modes. Figures 5(c)–5(f) correspond to the SW band structure evaluated at point P_4 but for different external field values. As observed, the asymmetry on the SW amplitudes remains unaltered under the modification of the external field. In the cases shown in Figs. 5(g)–5(j), the external field is fixed to $\mu_0 H_0 = 250$ mT, while the period of the system is varied (with $w = a/2$ for all cases). When the period increases the width of the Brillouin zones reduces, resulting in a limited dispersion of wave modes with more flat bands [72] than in the cases with varying magnetic fields. Alternatively, when the period is decreased, the width of the Brillouin zones increases, and the SWs within the BZ exhibit a more dispersive behavior, inhibiting the formation of flat bands. Concerning the amplitude of the simulated power spectrum, it is observed that the asymmetry is more pronounced as the period increases, where all the lowest-frequency flat modes start to become nonreciprocal. This behavior is due to the tendency of all flat bands to be localized beneath the HMs as a increases. Therefore, chiral MCs featuring a periodic DMI offer a remarkable capability of selective localization of the flat SW modes, demonstrating both reciprocal and nonreciprocal magnetization oscillations, depending on the interplay between anisotropy and DMI strength. Consequently, in addition to the nonreciprocity in frequency induced by DMI, the amplitude-based

nonreciprocity of flat modes emerges as an extra degree of freedom to effectively manipulate the dynamic characteristics of chiral magnonic crystals.

IV. CONCLUSIONS

This paper focused on the physics of magnonic flat bands and their nonreciprocal magnetization oscillation amplitudes in a nanoscale ferromagnetic film with periodic perpendicular anisotropy and interfacial Dzyaloshinskii-Moriya interaction. The study employed a localization diagram to examine the spatial confinement of magnonic modes in zones with and without DMI. The findings demonstrate the presence of flat modes with nonreciprocal amplitudes when SW localization occurs beneath the Pt nanowires, which is induced by the chiral Dzyaloshinskii-Moriya coupling. In contrast, when perpendicular anisotropy dominates, the flat modes localize in regions beneath the Ru nanowires, exhibiting a reciprocal amplitude. An analytical expression was derived to explain the selective localization of SW modes, establishing a relationship between anisotropy and interfacial DMI at the transition curve that separates the regions with SW modes localized in the zones with and without DMI. Micromagnetic simulations were conducted to verify the power-spectrum amplitude asymmetry of the flat modes, yielding perfect agreement with the theoretical predictions. This mechanism, linked to the amplitude asymmetry of flat magnonic bands, introduces an opportunity to enhance the control over SW excitations at the nanoscale. It opens up further opportunities for manipulating SWs, offering a promising alternative pathway for developing future magnon-based nanotechnological applications.

ACKNOWLEDGMENTS

The authors acknowledge financial support from Fondecyt Grants No. 1210607 and No. 1201153, and Basal Program for Centers of Excellence Grant No. AFB220001 CEDENNA (ANID-Chile). D.C.-O. acknowledges support by the DGIIE (UTFSM) through the Postdoctoral initiative. F.B. acknowledges ANID PhD through Fellowship No. 2021-21211469.

[1] A. G. Gurevich and G. A. Melkov, *Magnetization Oscillations and Waves* (CRC Press, Boca Raton, FL, 1996).
[2] S. Demokritov and A. Slavin, *Magnonics: From Fundamentals to Applications* (Springer, Berlin, 2012).
[3] S. M. Rezende, *Fundamentals of Magnonics*, Lecture Notes in Physics Vol. 969 (Springer, New York, 2020).
[4] M. Farle, Rep. Prog. Phys. **61**, 755 (1998).
[5] H. G. Bauer, P. Majchrak, T. Kachel, C. H. Back, and G. Woltersdorf, Nat. Commun. **6**, 8274 (2015).
[6] K. Ando, T. An, and E. Saitoh, Appl. Phys. Lett. **99**, 092510 (2011).
[7] H. Schultheiss, K. Vogt, and B. Hillebrands, Phys. Rev. B **86**, 054414 (2012).
[8] S. M. Mohseni, S. R. Sani, J. Persson, T. N. A. Nguyen, S. Chung, Y. Pogoryelov, P. K. Muduli, E. Iacocca, A. Eklund, R. K. Dumas *et al.*, Science **339**, 1295 (2013).
[9] M. Saravanan and A. Arnaudon, Phys. Lett. A **382**, 2638 (2018).
[10] F. Matsukura, Y. Tokura, and H. Ohno, Nat. Nanotechnol. **10**, 209 (2015).
[11] A. Barman, G. Gubbiotti, S. Ladak, A. O. Adeyeye, M. Krawczyk, J. Gräfe, C. Adelmann, S. Cotofana, A. Naeemi, V. I. Vasyuchka *et al.*, J. Phys.: Condens. Matter **33**, 413001 (2021).
[12] S. Neusser and D. Grundler, Adv. Mater. **21**, 2927 (2009).
[13] Á. Papp, W. Porod, and G. Csaba, Nat. Commun. **12**, 6422 (2021).
[14] H. Yu, O. d'Allivy Kelly, V. Cros, R. Bernard, P. Bortolotti, A. Anane, F. Brandl, F. Heimbach, and D. Grundler, Nat. Commun. **7**, 11255 (2016).
[15] K. Baumgaertl, J. Gräfe, P. Che, A. Mucchietto, J. Förster, N. Träger, M. Bechtel, M. Weigand, G. Schütz, and D. Grundler, Nano Lett. **20**, 7281 (2020).
[16] P. Pirro, V. I. Vasyuchka, A. A. Serga, and B. Hillebrands, Nat. Rev. Mater. **6**, 1114 (2021).
[17] K. Zakeri, Y. Zhang, J. Prokop, T.-H. Chuang, N. Sakr, W. X. Tang, and J. Kirschner, Phys. Rev. Lett. **104**, 137203 (2010).
[18] K. Di, V. L. Zhang, H. S. Lim, S. C. Ng, M. H. Kuok, J. Yu, J. Yoon, X. Qiu, and H. Yang, Phys. Rev. Lett. **114**, 047201 (2015).
[19] J. Cho, N.-H. Kim, S. Lee, J.-S. Kim, R. Lavrijsen, A. Solignac, Y. Yin, D.-S. Han, N. J. J. van Hoof, H. J. M. Swagten, B. Koopmans, and C.-Y. You, Nat. Commun. **6**, 7635 (2015).
[20] S. Tacchi, R. E. Troncoso, M. Ahlberg, G. Gubbiotti, M. Madami, J. Åkerman, and P. Landeros, Phys. Rev. Lett. **118**, 147201 (2017).
[21] S. Seki, Y. Okamura, K. Kondou, K. Shibata, M. Kubota, R. Takagi, F. Kagawa, M. Kawasaki, G. Tatara, Y. Otani, and Y. Tokura, Phys. Rev. B **93**, 235131 (2016).
[22] G. Gitgeatpong, Y. Zhao, P. Piyawongwatthana, Y. Qiu, L. W. Harriger, N. P. Butch, T. J. Sato, and K. Matan, Phys. Rev. Lett. **119**, 047201 (2017).
[23] I. Dzyaloshinsky, J. Phys. Chem. Solids **4**, 241 (1958).
[24] T. Moriya, Phys. Rev. Lett. **4**, 228 (1960).
[25] M. Kataoka, J. Phys. Soc. Jpn. **56**, 3635 (1987).
[26] L. Udvardi and L. Szunyogh, Phys. Rev. Lett. **102**, 207204 (2009).
[27] D. Cortés-Ortuño and P. Landeros, J. Phys.: Condens. Matter **25**, 156001 (2013).
[28] R. A. Gallardo, D. Cortés-Ortuño, R. E. Troncoso, and P. Landeros, in *Three-Dimensional Magnonics*, edited by G. Gubbiotti (Jenny Stanford Publishing, Berlin, 2019), pp. 121–160.
[29] M. Kuepferling, A. Casiraghi, G. Soares, G. Durin, F. Garcia-Sanchez, L. Chen, C. H. Back, C. H. Marrows, S. Tacchi, and G. Carlotti, Rev. Mod. Phys. **95**, 015003 (2023).
[30] K. Mika and P. Grünberg, Phys. Rev. B **31**, 4465 (1985).
[31] P. Grünberg, J. Appl. Phys. **57**, 3673 (1985).
[32] K. Di, S. X. Feng, S. N. Piramanayagam, V. L. Zhang, H. S. Lim, S. C. Ng, and M. H. Kuok, Sci. Rep. **5**, 10153 (2015).

[33] R. A. Gallardo, P. Alvarado-Seguel, T. Schneider, C. Gonzalez-Fuentes, A. Roldán-Molina, K. Lenz, J. Lindner, and P. Landeros, New J. Phys. **21**, 033026 (2019).

[34] R. A. Gallardo, T. Schneider, A. K. Chaurasiya, A. Oelschlägel, S. S. P. K. Arekapudi, A. Roldán-Molina, R. Hübner, K. Lenz, A. Barman, J. Fassbender, J. Lindner, O. Hellwig, and P. Landeros, Phys. Rev. Appl. **12**, 034012 (2019).

[35] R. A. Gallardo, P. Alvarado-Seguel, A. Kákay, J. Lindner, and P. Landeros, Phys. Rev. B **104**, 174417 (2021).

[36] P. I. Gerevenkov, V. D. Bessonov, V. S. Teplov, A. V. Telegin, A. M. Kalashnikova, and N. E. Khokhlov, Nanoscale **15**, 6785 (2023).

[37] J. A. Otálora, M. Yan, H. Schultheiss, R. Hertel, and A. Kákay, Phys. Rev. Lett. **117**, 227203 (2016).

[38] D. D. Sheka, O. V. Pylypovskyi, P. Landeros, Y. Gaididei, A. Kákay, and D. Makarov, Commun. Phys. **3**, 128 (2020).

[39] R. A. Gallardo, P. Alvarado-Seguel, and P. Landeros, Phys. Rev. B **105**, 104435 (2022).

[40] P. Landeros, J. A. Otálora, R. Streubel, and A. Kákay, in *Tubular Geometries*, edited by D. Makarov and D. D. Sheka (Springer International Publishing, Cham, 2022), pp. 163–213.

[41] R. Gallardo, P. Alvarado-Seguel, and P. Landeros, Phys. Rev. Appl. **18**, 054044 (2022).

[42] J. Lan, W. Yu, R. Wu, and J. Xiao, Phys. Rev. X **5**, 041049 (2015).

[43] N. Reiskarimian and H. Krishnaswamy, Nat. Commun. **7**, 11217 (2016).

[44] Q. Wang, A. V. Chumak, and P. Pirro, Nat. Commun. **12**, 2636 (2021).

[45] E. Albisetti, S. Tacchi, R. Silvani, G. Scaramuzzi, S. Finizio, S. Wintz, C. Rinaldi, M. Cantoni, J. Raabe, G. Carlotti *et al.*, Adv. Mater. **32**, 1906439 (2020).

[46] K. Szulc, P. Graczyk, M. Mruczkiewicz, G. Gubbiotti, and M. Krawczyk, Phys. Rev. Appl. **14**, 034063 (2020).

[47] M. Grassi, M. Geilen, D. Louis, M. Mohseni, T. Brächer, M. Hehn, D. Stoeffler, M. Bailleul, P. Pirro, and Y. Henry, Phys. Rev. Appl. **14**, 024047 (2020).

[48] J. Chen, H. Yu, and G. Gubbiotti, J. Phys. D: Appl. Phys. **55**, 123001 (2022).

[49] V. V. Kruglyak, S. O. Demokritov, and D. Grundler, J. Phys. D: Appl. Phys. **43**, 264001 (2010).

[50] B. Lenk, H. Ulrichs, F. Garbs, and M. Münzenberg, Phys. Rep. **507**, 107 (2011).

[51] H. Yu, G. Duerr, R. Huber, M. Bahr, T. Schwarze, F. Brandl, and D. Grundler, Nat. Commun. **4**, 2702 (2013).

[52] G. Gubbiotti, S. Tacchi, M. Madami, G. Carlotti, A. O. Adeyeye, and M. Kostylev, J. Phys. D: Appl. Phys. **43**, 264003 (2010).

[53] M. Krawczyk and D. Grundler, J. Phys.: Condens. Matter **26**, 123202 (2014).

[54] S. Tacchi, G. Gubbiotti, M. Madami, and G. Carlotti, J. Phys.: Condens. Matter **29**, 073001 (2017).

[55] K.-S. Lee, D.-S. Han, and S.-K. Kim, Phys. Rev. Lett. **102**, 127202 (2009).

[56] A. V. Chumak, V. I. Vasyuchka, A. A. Serga, and B. Hillebrands, Nat. Phys. **11**, 453 (2015).

[57] A. V. Chumak, A. A. Serga, and B. Hillebrands, J. Phys. D: Appl. Phys. **50**, 244001 (2017).

[58] I. Barsukov, F. M. Römer, R. Meckenstock, K. Lenz, J. Lindner, S. Hemken to Krax, A. Banholzer, M. Körner, J. Grebing, J. Fassbender, and M. Farle, Phys. Rev. B **84**, 140410(R) (2011).

[59] P. Landeros and D. L. Mills, Phys. Rev. B **85**, 054424 (2012).

[60] M. Körner, K. Lenz, R. A. Gallardo, M. Fritzsche, A. Mücklich, S. Facsko, J. Lindner, P. Landeros, and J. Fassbender, Phys. Rev. B **88**, 054405 (2013).

[61] R. A. Gallardo, A. Banholzer, K. Wagner, M. Körner, K. Lenz, M. Farle, J. Lindner, J. Fassbender, and P. Landeros, New J. Phys. **16**, 023015 (2014).

[62] G. Gubbiotti, L. L. Xiong, F. Montoncello, and A. O. Adeyeye, Appl. Phys. Lett. **111**, 192403 (2017).

[63] Z. K. Wang, V. L. Zhang, H. S. Lim, S. C. Ng, M. H. Kuok, S. Jain, and A. O. Adeyeye, Appl. Phys. Lett. **94**, 083112 (2009).

[64] Z. K. Wang, V. L. Zhang, H. S. Lim, S. C. Ng, M. H. Kuok, S. Jain, and A. O. Adeyeye, ACS Nano **4**, 643 (2010).

[65] S. Tacchi, G. Duerr, J. W. Kłos, M. Madami, S. Neusser, G. Gubbiotti, G. Carlotti, M. Krawczyk, and D. Grundler, Phys. Rev. Lett. **109**, 137202 (2012).

[66] M. Krawczyk, S. Mamica, M. Mruczkiewicz, J. W. Kłos, S. Tacchi, M. Madami, G. Gubbiotti, G. Duerr, and D. Grundler, J. Phys. D: Appl. Phys. **46**, 495003 (2013).

[67] G. Gubbiotti, X. Zhou, Z. Haghshenasfard, M. G. Cottam, and A. O. Adeyeye, Phys. Rev. B **97**, 134428 (2018).

[68] P. Alvarado-Seguel and R. A. Gallardo, Phys. Rev. B **100**, 144415 (2019).

[69] T. Yu, Z. Luo, and G. E. Bauer, Phys. Rep. **1009**, 1 (2023).

[70] R. A. Gallardo, D. Cortés-Ortuño, T. Schneider, A. Roldán-Molina, F. Ma, R. E. Troncoso, K. Lenz, H. Fangohr, J. Lindner, and P. Landeros, Phys. Rev. Lett. **122**, 067204 (2019).

[71] J. Flores-Farías, R. A. Gallardo, F. Brevis, A. Roldán-Molina, D. Cortés-Ortuño, and P. Landeros, Sci. Rep. **12**, 17831 (2022).

[72] S. Tacchi, J. Flores-Farías, D. Petti, F. Brevis, A. Cattoni, G. Scaramuzzi, D. Girardi, D. Cortés-Ortuño, R. A. Gallardo, E. Albisetti *et al.*, Nano Lett. **23**, 6776 (2023).

[73] F. Ma and Y. Zhou, RSC Adv. **4**, 46454 (2014).

[74] H. Yang, A. Thiaville, S. Rohart, A. Fert, and M. Chshiev, Phys. Rev. Lett. **115**, 267210 (2015).

[75] W. Zhang, R. Chen, B. Jiang, X. Zhao, W. Zhao, S. S. Yan, G. Han, S. Yu, G. Liu, and S. Kang, Nanoscale **13**, 2665 (2021).

[76] S. K. Jena, R. Islam, E. Milińska, M. M. Jakubowski, R. Minikayev, S. Lewińska, A. Lynnyk, A. Pietruczik, P. Aleszkiewicz, C. Autieri, and A. Wawro, Nanoscale **13**, 7685 (2021).

[77] Z. Zhou, P. Marcon, X. Devaux, P. Pigeat, A. Bouché, S. Migot, A. Jaafar, R. Arras, M. Vergnat, L. Ren *et al.*, ACS Appl. Mater. Interfaces **13**, 32579 (2021).

[78] L. Cestarollo, K. Srinivasan, and A. El-Ghazaly, J. Magn. Magn. Mater. **562**, 169825 (2022).

[79] D. Odkhuu, S. H. Rhim, N. Park, K. Nakamura, and S. C. Hong, Phys. Rev. B **91**, 014437 (2015).

[80] A. G. Kolesnikov, M. E. Stebliy, A. V. Ognev, A. S. Samardak, A. N. Fedorets, V. S. Plotnikov, X. Han, and L. A. Chebotkevich, J. Phys. D: Appl. Phys. **49**, 425302 (2016).

[81] M. Belmeguenai, H. Bouloussa, Y. Roussigné, M. S. Gabor, T. Petrisor, C. Tiusan, H. Yang, A. Stashkevich, and S. M. Chérif, Phys. Rev. B **96**, 144402 (2017).

[82] M. Belmeguenai, D. Apalkov, M. Gabor, F. Zighem, G. Feng, and G. Tang, IEEE Trans. Magn. **54**, 1 (2018).

[83] A. Ruiz-Calaforra, T. Brächer, V. Lauer, P. Pirro, B. Heinz, M. Geilen, A. V. Chumak, A. Conca, B. Leven, and B. Hillebrands, J. Appl. Phys. **117**, 163901 (2015).

[84] A. Conca, B. Heinz, M. R. Schweizer, S. Keller, E. T. Papaioannou, and B. Hillebrands, Phys. Rev. B **95**, 174426 (2017).

[85] B. W. Zingsem, M. Farle, R. L. Stamps, and R. E. Camley, Phys. Rev. B **99**, 214429 (2019).

[86] J. Kisielewski, P. Gruszecki, M. Krawczyk, V. Zablotskii, and A. Maziewski, Phys. Rev. B **107**, 134416 (2023).

[87] R. Silvani, M. Kuepferling, S. Tacchi, and G. Carlotti, J. Magn. Magn. Mater. **539**, 168342 (2021).